ADVANCED MATERIALS
www.advmat.de

# Electrically Tunable Friction: From Sticky to Slippery with Ionic Hydrogels

*Chenxu Liu, Yuan Yao, Yuanyuan Wang, Qi Zhou, Ziqian Zhao, Chenyu Qiao, Yongxiang Sun, Yonggang Meng, Yu Tian,* and Hongbo Zeng**

**Real-time regulation of friction from conventional dry states to ultra-low levels represents a critical strategy for improving energy efficiency and enabling the intelligent design of adaptive systems. Yet, current friction-control methods typically achieve only modest modulation and often rely on liquid lubricants at macroscopic scales, which impose stringent sealing requirements and limit practical applications. Here, an electric-field strategy is reported for friction modulation using a polyvinyl alcohol-based ionic hydrogel as an electroresponsive frictional material. During sliding against a metal ball, the friction coefficient (COF) can be reversibly modulated by more than fifty-fold under low voltage control (−30 V to +30 V), without the need for external lubricants. Remarkably, the COF decreases to 0.03 at −30 V (with the metal ball connected to the negative pole), while at 0 V or +30 V it increases to 1–2. Mechanistic analyses reveal that positive charging of the ionic hydrogel triggers electroosmotic extraction of a salt-rich interfacial layer, driving the dramatic reduction in friction. It further demonstrates the first crawling robot and precision robotic arm manipulation powered by electrotunable friction, establishing a new paradigm for adaptive and energy-efficient robotic and mechanical systems.**

## 1. Introduction

Tribology, encompassing friction, wear, and lubrication, is integral to modern life, influencing energy efficiency, maintenance intervals, machine components, and overall quality of life.[1,2] Remarkably, ≈23% of the world's total energy consumption stems from tribological contacts.[3] Reducing friction-induced losses and minimizing wear are critical challenges in tribology. Achieving ultra-low friction (coefficient of friction (COF) ≤0.03), or even superlubricity (COF<0.01), has become a central goal in tribology, with significant process reported in areas such as liquid superlubricity[4–8] and structural superlubricity.[9–11]

For practical applications, the ability to actively control ultra-low friction or superlubricity is crucial, as it allows for adaptive friction management under varying operational conditions. Traditional tribological contacts are typically passive, with predetermined geometry, materials, and lubricants fixed during the design and manufacturing phases.[12] These systems lack real-time adjustability, making them highly sensitive to harsh or changing operating conditions. When lubrication deteriorates during operation, their performance declines due to an inability to adapt. To address this limitation, active tribology, also known as tribotronics,[13] has emerged as a promising approach. Tribotronics introduces real-time adjustability in tribological systems, allowing them to respond dynamically to changing conditions without requiring alterations in design or materials.

Among the active control methods for friction and wear, techniques employing external fields, such as optical fields[14] and magnetic or electric fields,[15] has drawn increasing attention. Of these, electric field-controlled friction has emerged as a particularly promising approach due to the ease and precision of applying electricity.[16–20] These studies highlight the versatility of electric field-controlled friction and its potential for various applications, spanning from tribological systems to interactive tactile devices. With the advancement of nanotechnology, research on electric field-controlled friction has significantly progressed at the micro- and nanoscale, driven by the development of tools such as atomic force microscopy (AFM)[21,22] and surface force apparatus (SFA).[6,16] These nanofriction studies have elucidated several mechanisms, including electrochemical reactions, electroadsorption/desorption, and material orientation changes.[23,24] More recently, sliding friction between lipid-bilayer-coated surfaces was shown, via a nanofriction experiment using a surface

C. Liu, Y. Yao, Y. Wang, Q. Zhou, Z. Zhao, C. Qiao, Y. Sun, H. Zeng
Department of Chemical and Materials Engineering
University of Alberta
Edmonton, AB T6G 1H9, Canada
E-mail: hongbo.zeng@ualberta.ca
C. Liu, Y. Meng, Y. Tian
State Key Laboratory of Tribology in Advanced Equipment
Tsinghua University
Beijing 100084, China
E-mail: tianyu@mail.tsinghua.edu.cn

The ORCID identification number(s) for the author(s) of this article can be found under https://doi.org/10.1002/adma.202518350



**DOI: 10.1002/adma.202518350**

force balance, to be reversibly modulated by transmembrane electric fields, with variations reaching up to 200-fold.[6]

Although substantial progress has been achieved at the nanoscale, controlling friction force or COF under macroscopic conditions remains highly restricted.[22,25–27] Typically, electric field modulation of COF in macroscale systems achieves only a few multiples of variation and rarely exceeds one order of magnitude.[19,23,28] Moreover, existing studies predominantly rely on lubrication-based strategies.[16] However, liquid lubrication introduces significant challenges, such as sealing issues and the risk of material corrosion, which severely constrain its practical applications.

Achieving in situ regulation of the COF at macroscales, ranging from traditional dry friction to ultra-low friction, could revolutionize electronic friction control applications. This work addresses these gaps by pioneering the discovery of electrotunable friction between ionic hydrogels and metal surfaces in the absence of external liquid lubricants. At a safe voltage of −30 V (with the metal ball contacted to the negative pole), the COF decreases to as low as 0.03, whereas at 0 V or +30 V, it increases to 1–2. This demonstrates an unprecedented more-than-fifty-fold modulation of the COF at the macroscopic scale. Ionic hydrogels are widely utilized in applications such as electroactive actuators,[29,30] represented by artificial muscles or ionic skin, and flexible sensors.[31,32] Achieving precise and adaptive friction control between ionic hydrogels and metals holds significant potential for advancing robotic systems and sensing technologies.

## 2. Results and Discussion

### 2.1. Design Concept of Electrotunable Friction

Dynamic control of friction is essential for managing start-stop motion in both industrial settings and everyday situations. For instance, a person maintains stability when the friction between their feet and the ground is high, while insufficient friction increases the risk of slipping. Similar principles apply to systems that require transitions between high and low friction, such as pulley mechanisms, ship launching operations, and robotic arm manipulation. Furthermore, inspired by the locomotion of insects and the soft robots,[33–36] a crawling robot consisting of a head, a tail, and a telescopic brake can be designed. As shown in **Figure 1a**, when the friction between the head and the ground is low while that of the tail is high, the head moves forward; conversely, when the friction at the tail decreases and is lower than that at the head, the tail advances. This differential friction mechanism enables effective and adaptive movement.

Currently, most friction control strategies rely on liquid lubricants.[19,20,28] However, to realize the crawling robot design shown in Figure 1a, it is crucial to develop methods for real-time friction control under dry conditions without external liquid lubrication. Leveraging recent advances in ionic hydrogels,[37] we propose a novel approach: using electric fields to regulate the lubricating substances at the contact interface between ionic hydrogels and metals. This method enables precise control of friction, opening new possibilities for innovative applications in systems that require adaptive friction management.

Polyvinyl alcohol (PVA) polymer doped with lithium bis(trifluoromethane)sulfonimide (LiTFSI) was selected as the friction material, with its structural schematic shown in Figure 1b. PVA is widely used in hydrogel lubricating layers due to its high hydrophilicity, particularly in applications such as artificial cartilage replacement. Although PVA hydrogels with high water content exhibit excellent biocompatibility, chemical stability, and mechanical strength, they suffer from inadequate lubrication due to strong intermolecular hydrogen bonding.[38] Therefore, LiTFSI is utilized as a lubricant additive to improve both the lubricating performance and electric field response of PVA in this work.

By employing PVA/LiTFSI and metal as both the frictional counterparts and electrodes, we investigated the underlying mechanism and preliminary outcomes of friction regulation under various electric fields. Figure 1c presents a schematic illustration of electrotunable friction during the sliding of the ionic hydrogel against a metal ball under different electric fields. In the absence of an applied electric field, anions and cations in the ionic hydrogel are randomly distributed. However, under either a positive or negative electric field, the LiTFSI doped in the hydrogel migrates under the influence of the electric field, forming a directional distribution of charged particles at the friction interface between the metal ball and the PVA material. For instance, when the metal surface is negatively charged and the PVA is positively charged, $TFSI^-$ is primarily concentrated on the lower friction pair surface due to electrostatic interactions, while $Li^+$ is mainly distributed near the metal ball (negative pole). Conversely, the opposite distribution occurs when the polarity is reversed. When the metal ball is connected to the positive pole, it is more prone to chemical or electrochemical reactions with $H_2O$ and/or $O_2$ in the air, resulting in surface oxidation.

The force-time curves in Figure 1d show the variation of friction force between the ionic hydrogel and metal over time at different voltages. The results indicate that the friction force can be controlled to ±40 mN or ±0.8 mN by simply adjusting the applied voltage without changing the material composition or other experimental parameters of the friction system. Thus, friction control can be achieved either between negative voltage and zero voltage or between negative and positive voltages. More specific details are provided in Figure S1 (Supporting Information) and the following sections.

### 2.2. Preparation and Characterization of Ionic Hydrogels

The ionic hydrogel was prepared using a simple one-pot method, where PVA and LiTFSI were dissolved in water and then subjected to a freeze-thaw process. This resulted in a clear, transparent, and uniform hydrogel, referred to PVA/$LiTFSI_x$, with "x" representing the LiTFSI content. LiTFSI is dispersed in PVA at molecular level and destroys the PVA crystallites because of the interaction between the salt and hydroxyl groups in PVA. In addition, it is expected that $Li^+$ acts as the crosslinking point between the PVA chains, resulting in a network of amorphous PVA chains.

**Figure 2a** presents the X-ray diffraction (XRD) analysis used to examine the structural changes in PVA induced by the incorporation of LiTFSI. For pure PVA, a sharp diffraction peak is observed at $2\theta = 21°$, corresponding to the (101) crystalline plane. Pure LiTFSI also exhibits distinct crystalline peaks, as

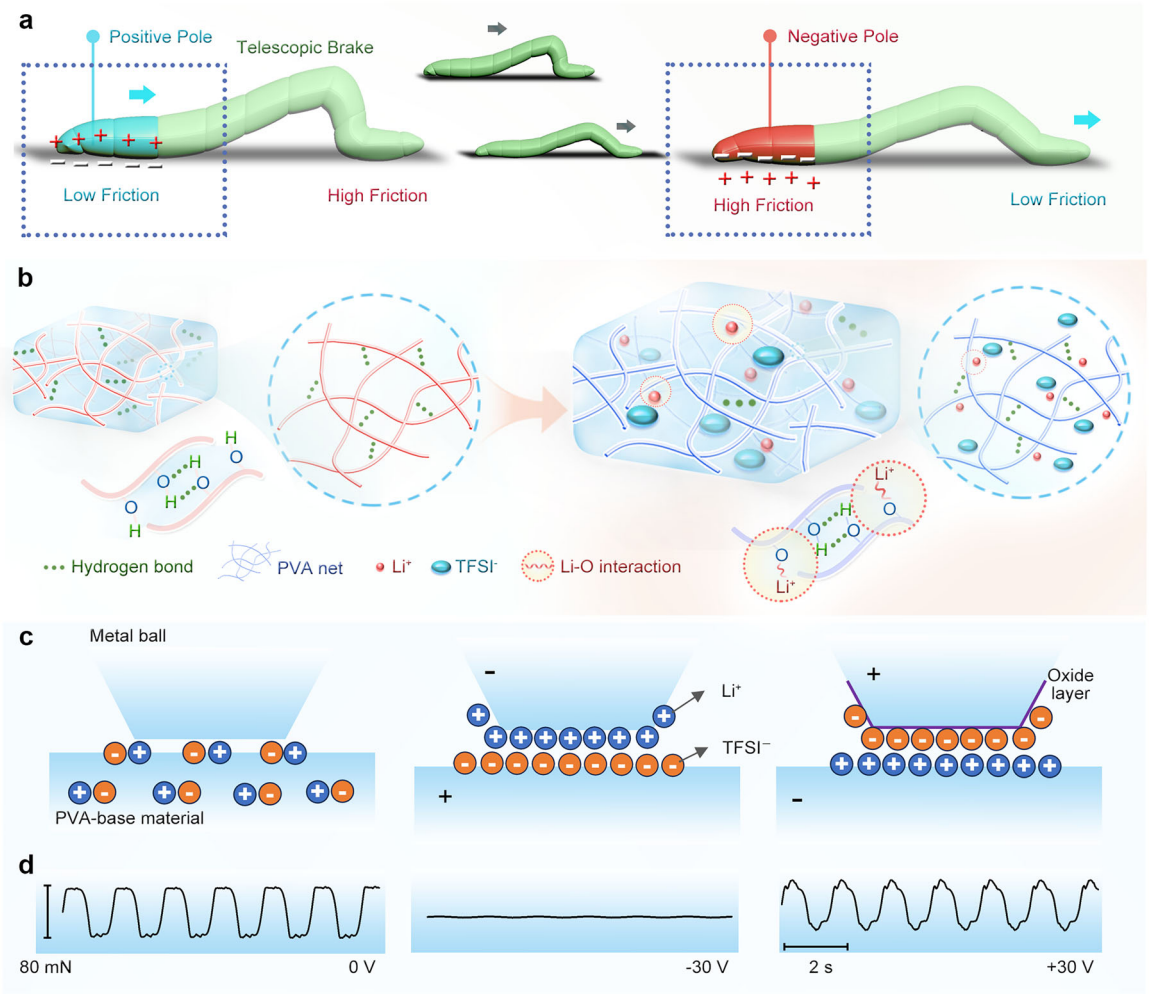


**Figure 1.** Schematic illustration of potential applications and design principles of electrotunable friction: a) Schematic of a crawling robot inspired by worm-like peristaltic motion and electrotunable friction; b) Structural diagram of the PVA/LiTFSI via freeze-thaw cycling, driven by hydrogen bonding and Li—O interactions; c) Illustration of friction modulation between an ionic hydrogel and a metal ball under different electric fields. Proposed mechanism: when the ionic hydrogel is connected as the anode and the metal ball as the cathode, a removable boundary film forms on the metal surface. In contrast, connecting the metal ball as the anode leads to the formation of an oxide film; d) Time-dependent friction force between the PVA/LiTFSI versus a metal ball with a diameter of 2 mm at various voltages. Experiments were conducted under a normal load of 20 mN and a sliding velocity of 2 mm $s^{-1}$.

shown in Figure S2 (Supporting Information). With increasing salt concentration, the intensity of the PVA diffraction peaks decreases, and the peak width (full width at half maximum, FWHM) gradually increases. Notably, no LiTFSI diffraction peaks are observed in the composite films, indicating that the salt is fully dissociated at even 50 wt.% and its ions are strongly coordinated with the hydroxyl groups of PVA.[39] The addition of LiTFSI also improved the polymer's optical properties. All PVA/LiTFSI polymers were highly transparent, achieving over 80% transmittance in the 400–800 nm range (Figure S3, Supporting Information), which was higher than that of pure PVA films. This enhanced transparency was due to the amorphous structure formed during freezing, as polymer chains became more evenly distributed, leading to better optical clarity with increasing LiTFSI concentration.

Fourier transform infrared spectroscopy (FTIR) analysis (Figure S4, Supporting Information) further shows the interaction between PVA and LiTFSI. For pure PVA, the characteristic absorption peaks are at 3250 $cm^{-1}$ for O—H stretching, 2906–2936 $cm^{-1}$ for asymmetric stretching and symmetric stretching of $CH_2$, 1660 $cm^{-1}$ due to water absorption, 1410–1460 $cm^{-1}$ for C—H bending, 1327 $cm^{-1}$ for $\delta$(OH), 1087 $cm^{-1}$ for bending of OH, 914 $cm^{-1}$ for $CH_2$ rocking, and 833 $cm^{-1}$ for C—C stretching.[40,41] For LiTFSI doped PVA, in addition to the aforementioned characteristic peaks, the characteristic peaks also include 1347 $cm^{-1}$ for asymmetric $SO_2$ stretching, 1185 $cm^{-1}$ for asymmetric stretching mode of $CF_3$, 1132 $cm^{-1}$ for C—$SO_2$—N bonding mode, 1053 $cm^{-1}$ for asymmetric S-N-S stretching mode of LiTFSI.[42] As the LiTFSI concentration increases, the hydrogen-bonded O—H peak gradually diminishes, while the free O—H peak becomes more prominent (Figures S5 and S6, Supporting Information), indicating that LiTFSI disrupts the hydrogen-bonding network and releases more free hydroxyl groups within the hydrogel.[43] This trend reflects a weakening of

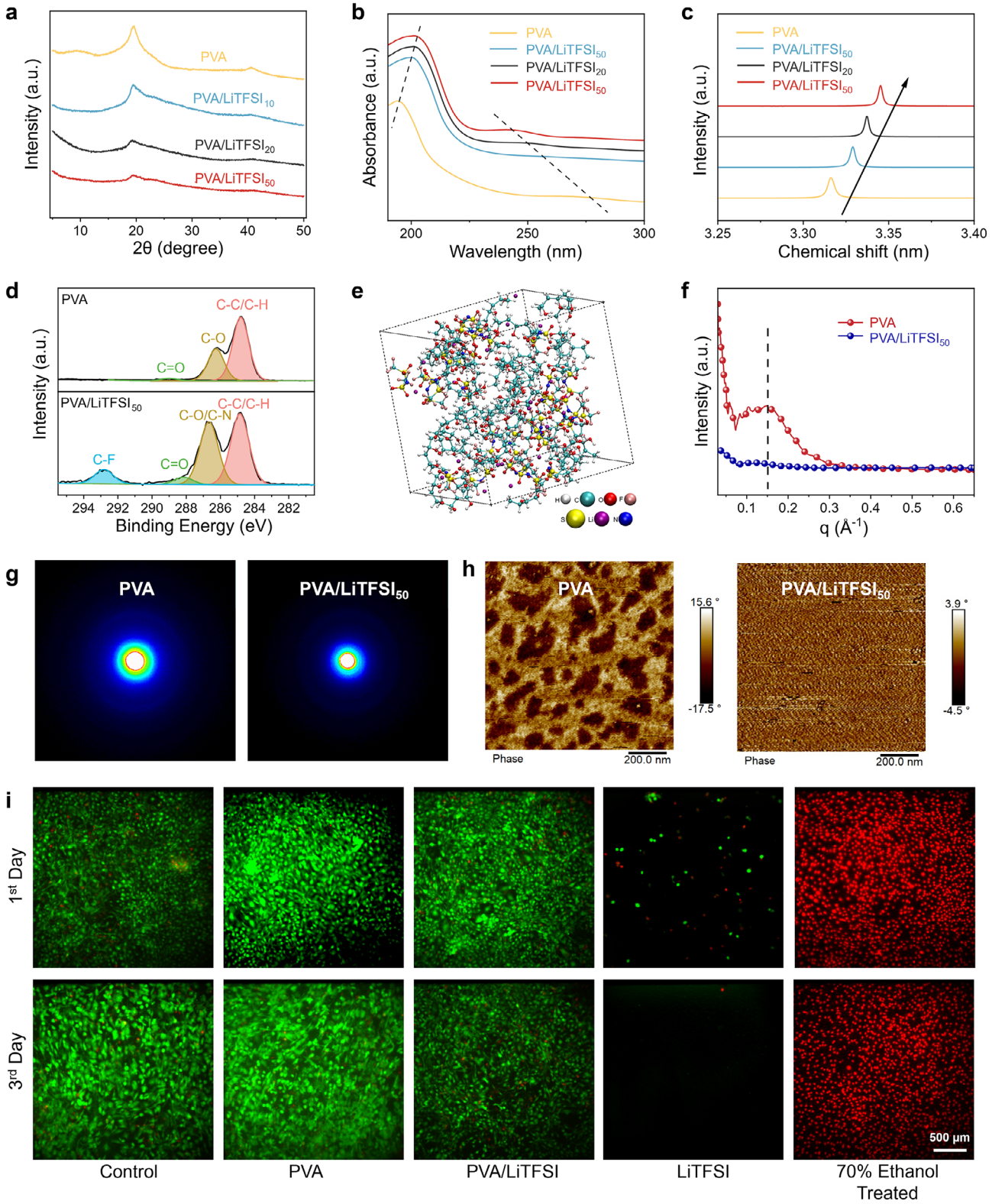


**Figure 2.** Characterization of PVA and PVA/LiTFSI. a) XRD patterns of PVA and PVA/LiTFSI; b) UV–vis absorption spectra of PVA and PVA/LiTFSI; c) $^{1}$H-NMR spectra of PVA and PVA/LiTFSI; d) XPS C 1s spectra of PVA/LiTFSI; e) Snapshots from molecular dynamics simulations of PVA/LiTFSI; SAXS profiles of PVA and PVA/LiTFSI f) and their corresponding 2D SAXS patterns (g); h) AFM phase images of pure PVA coating and PVA/LiTFSI$_{50}$ coating; i) NIH/3T3 cell live/dead staining image.

hydrogen-bond interactions in the ionic hydrogel and an increase in the number of unbound hydroxyl groups.

UV–vis spectroscopy reveals that LiTFSI alters the electronic structure of PVA. As shown in Figure 2b, pure PVA exhibits absorption peaks at 195 nm (n→$\pi$*) and 270 nm ($\pi$→$\pi$*), which shift to 200 nm (red shift) and 243 nm (blue shift), respectively, in the PVA/LiTFSI$_{50}$. The red shift suggests the formation of localized states within the bandgap, while the blue shift is likely attributed to Li—O interactions that disrupt PVA's hydrogen bonding.[44] This interpretation is further supported by $^{1}$H nuclear magnetic resonance (NMR) results (Figure 2c), where the proton peak of $H_2O$ shifts upfield with increasing LiTFSI concentration, indicating the weakening of hydrogen bonding between $H_2O$ and PVA.[45]

X-ray photoelectron spectroscopy (XPS) further confirms the incorporation of LiTFSI. Compared to pure PVA, the PVA/LiTFSI$_{50}$ spectrum (Figure S7, Supporting Information) displays distinct Li 1s and F 1s signals. The high-resolution C 1s spectrum (Figure 2d) reveals a new C-F peak at 285.2 eV, consistent with the presence of fluorine detected in the F 1s region.[46] Thermogravimetric analysis (TGA) results (Figure S8, Supporting Information) show that the addition of LiTFSI reduces the thermal stability of PVA, with the decomposition temperature of the PVA/LiTFSI$_{50}$ film decreasing from 257 °C (pure PVA) to 249 °C. This reduction correlates with decreased crystallinity, further supporting molecular-level interactions between LiTFSI and the PVA matrix.[47]

Molecular dynamics (MD) simulations (Figure 2e) reveal the presence of nonbonding interactions within the hydrogel system. The interaction distance between $H_2O$ molecules and PVA hydroxyl groups (≈1.9 Å) confirms hydrogen bonding, while additional van der Waals forces are observed at ≈3 Å (Figure S9a, Supporting Information).[48] The simulations also show that PVA chains are surrounded by LiTFSI molecules, further supporting their role in modifying the hydrogel network (Figure S9b, Supporting Information). In contrast, the radial distribution function characterizing the anion environment appears featureless; the gN-C(rd) function approaches unity, with only a broad shoulder ≈ 6 Å, as shown in Figure S9c (Supporting Information).[49] To further examine the microstructure of PVA and PVA/LiTFSI$_{50}$, small-angle X-ray scattering (SAXS) was employed. The result shows that the pure PVA exhibits a broad peak—known as the long period peak ($L = 2\pi/q_m$) —associated with the spacing between stacked lamellar crystals. The disappearance of this peak after LiTFSI incorporation indicates that strong Li-PVA interactions significantly disrupt the original hydrogel structure (Figure 2f,g).

The phase information in AFM imaging reflects local stiffness variations within the PVA samples without and with LiTFSI (Figure 2h). Crystallized regions, being more ordered and stiffer than amorphous domains, appear as brighter areas in the phase contrast images, while the softer amorphous regions appear darker. This contrast arises from differences in mechanical response due to hydrogel crystallization. Notably, the microphase domain sizes estimated from AFM line profiles are consistent with SAXS results, showing a similar trend in structural variation. The surface roughness (Ra) values of PVA and PVA/LiTFSI$_{50}$ coatings on silicon wafers are 1.46 and 0.66 nm, respectively, indicating smooth and uniform surfaces at the nanoscale and ruling out topographical contributions to the observed contrast (Figure S10, Supporting Information). SEM images (Figure S11, Supporting Information) reveal that PVA/LiTFSI$_{50}$ films exhibit a denser microporous structure compared to the more loosely packed pure PVA, suggesting that LiTFSI serves as a physical cross-linking agent. Energy-dispersive X-ray (EDX) elemental mapping (Figure S12, Supporting Information) shows a uniform elemental distribution.

The mechanical properties of the ionic hydrogel are evaluated using rheological and tensile tests. Time sweeping results in Figure S13a (Supporting Information) show that the storage modulus (G′) consistently exceeds the loss modulus (G″), indicating solid-like behavior and structural stability. In strain sweep tests, both moduli remain constant within the linear viscoelastic region, while G′ decreases at higher strains, reflecting network disruption (Figure S13b, Supporting Information). Frequency sweep tests further confirm the material's stability, showing no G′/G″ crossover and frequency-independent behavior at low frequencies, which suggests long-term structural integrity (Figure S13c, Supporting Information). This stability arises from reversible physical crosslinking and the mobility of hydrogel chain segments, allowing the polymer to endure dynamic conditions. Cyclic strain tests demonstrate rapid recovery of G′, highlighting a strong self-healing ability (Figure S13d, Supporting Information), which is especially advantageous in applications involving repeated friction. Tensile tests (Figure S14, Supporting Information) show that LiTFSI incorporation increases the elongation at break from 720% to 2370%, while reducing the tensile strength from 2.36 MPa to 0.57 MPa. This increase in stretchability results from LiTFSI-induced expansion of the hydrogel network, enhancing flexibility. Such flexibility helps mitigate frictional stress and contributes to stable frictional performance. In addition, adhesion is critical for maintaining stable contact between the ionic hydrogel coating and the substrate (e.g., glass slide). PVA/LiTFSI$_{50}$ shows strong adhesion across various materials, with significantly higher peeling strength than pure PVA due to weakened crystallinity and enhanced reversible interactions.

In mechanical behaviors involving contact with biological tissues or the human body, biocompatibility is a critical concern, especially given the potential health risks associated with prolonged exposure to LiTFSI. Live/dead staining (Figure 2i) reveals that both PVA and PVA/LiTFSI$_{50}$ maintain high cell viability, whereas pure LiTFSI induces significant cell damage, likely due to osmotic imbalance. Methyl thiazolyl tetrazolium (MTT) assay results (Figure S15, Supporting Information) further confirm biocompatibility, with cell viabilities above 70%. These findings highlight the suitability of PVA/LiTFSI$_{50}$ for safe, long-term use in biocompatible tribosystems. Furthermore, to assess the suitability of ionic hydrogels for use in extreme cold, such as aerospace or polar regions, we evaluated their freezing resistance. At −18 °C, pure PVA turned white due to ice crystal formation, while PVA/LiTFSI$_{50}$ remained transparent, indicating suppressed crystallization (Figure S16a, Supporting Information). Differential scanning calorimetry (DSC) results confirmed that LiTFSI lowers the freezing point to −28 °C and reduces the melting peak (Figure S16b, Supporting Information). Unlike PVA, which becomes brittle, PVA/LiTFSI$_{50}$ remains flexible at low temperatures (Figure S17, Supporting Information). The

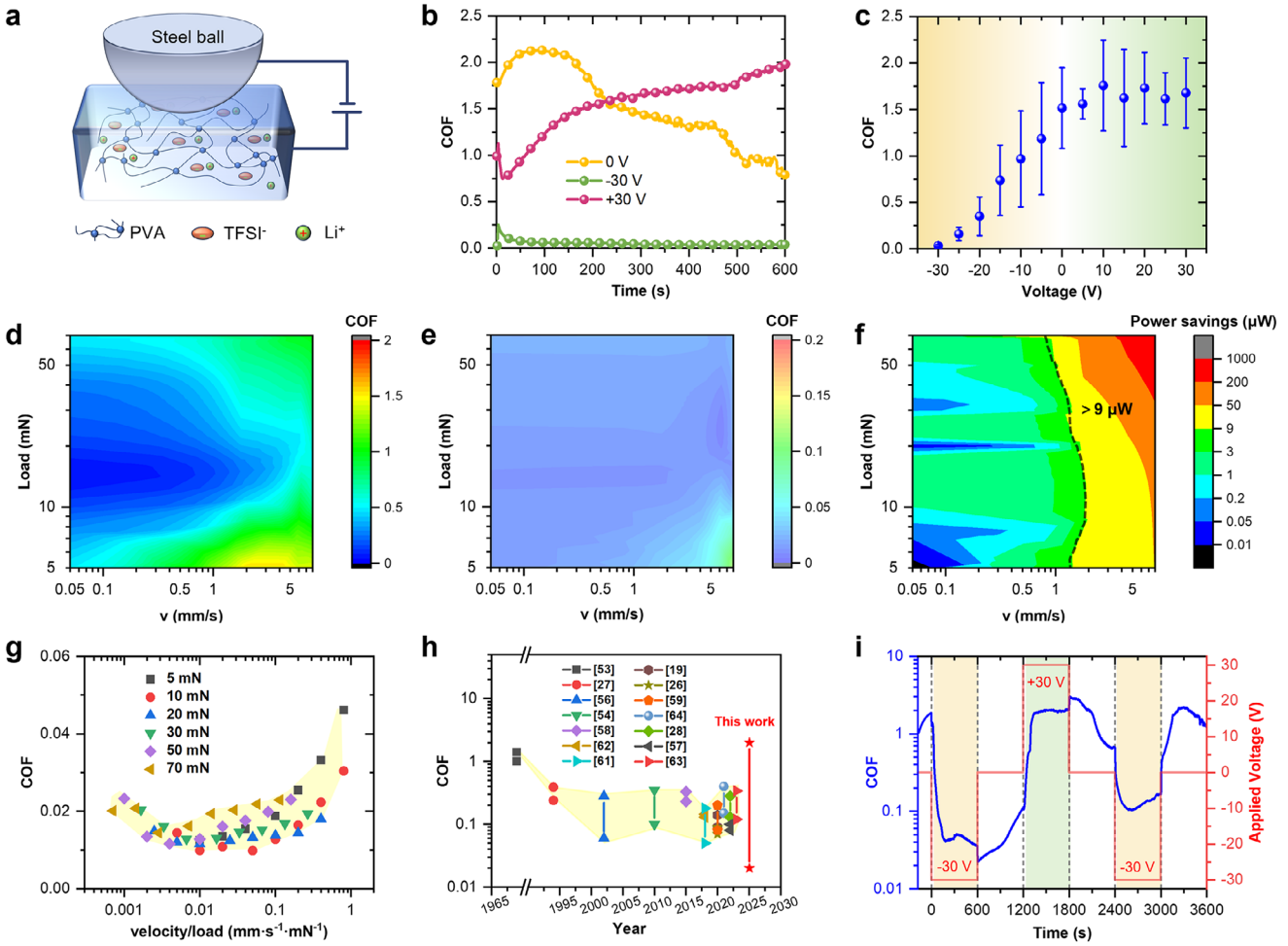


**Figure 3.** Schematic and tribological results of dry sliding tests between the PVA/LiTFSI and steel balls under different voltages: a) Schematic illustration of electrotunable friction, in which ionic hydrogels with a water content of 20–67% act as both the positive electrode and the lower friction pair, while a steel ball serves as the negative electrode and the upper friction pair; b) The COF during friction tests under different voltages. The tests were conducted under a load of 20 mN, a duration of 600 s, a sliding velocity of 2 mm $s^{-1}$, and at room temperature; c) Influence of voltage on the COF of PVA/$LiTFSI_{50}$ versus steel ball, measured at a sliding velocity of 2 mm $s^{-1}$ and a load of 5 mN; d) Influence of velocity and load on the COF in the absence of an applied voltage; e) Influence of velocity and load on the COF under an applied voltage of −30 V; f) Power savings resulting from the reduction in friction force before and after applying a −30 V voltage at different velocity and load. 9 μW is the power consumed for friction control under −30 V; g) The relationship between the velocity/load and the COF under an applied voltage of −30 V; h) Comparison with previous studies: the x-axis shows the publication year, and the y-axis indicates the range of COF variation induced by electric field control at the macroscopic scale; i) The time-dependent COF curve under alternating voltages of ±30 and 0 V.

excellent biocompatibility and freeze resistance of PVA/$LiTFSI_{50}$ ionic hydrogels make them highly suitable for special applications in both biomedical and extreme low-temperature environments.

### 2.3. Frictional Behaviors under External Voltage Control

The friction behavior of the ionic hydrogel was investigated under various applied voltages using a bearing steel ball as the counterpart. The schematic of electrotunable friction is shown in **Figure** 3a. In the absence of voltage, the COF is ≈2.0 and gradually decreases to ≈ 1.0 over time due to water loss from the ionic hydrogel. When the ionic hydrogel is connected as the anode and the steel ball as the cathode, the system reaches an ultra-low friction state with a COF of ≈0.03 at −30 V (Figure 3b). A similar phenomenon has also been observed when a titanium alloy ball replaces the steel ball as the counterpart (as shown in Figure S18, Supporting Information).

The effects of different voltages on the COF between the ionic hydrogel and the steel ball was further investigated as shown in Figure 3c. As the voltage becomes increasingly negative, the COF decreases from 1.52 ± 0.43 at 0 V to 0.03 ± 0.01 at −30 V. When the voltage varies continuously, the COF also changes accordingly. In Figure S19a (Supporting Information), when the voltage is held at 0 V for 120 s and then decreased by 5 V every 60 s, the COF decreases from 1.2–1.5. Between 420 and 480 s, the COF reaches a minimum value. Subsequently, as the voltage is increased by 5 V every 60 s, the COF begins to rise gradually. Figure S19b (Supporting Information) illustrates the COF

when the voltage is gradually increases from 0 to 30 V and then decreased back to 0 V. When the steel ball is connected to the positive pole, the COF increases with increasing voltage and decreases with decreasing voltage.

In addition, we examined the electrotunable friction behavior of a different PVA-based ionic hydrogel paired with the steel ball. Replacing the LiTFSI-doped PVA-based ionic hydrogel with an $NH_4Cl$-doped PVA-based ionic hydrogel yielded similar trends (Figures S20 and S21, Supporting Information): the COF decreases under negative voltage and increases under positive voltage. Meanwhile, the effect of an external electric field during the sliding between pure PVA and a steel ball was investigated under the same conditions. As shown in Figure S22 (Supporting Information), when the steel ball was connected to the negative electrode, the COF exhibited a slight decrease but not as significant as when PVA/LiTFSI or PVA/$NH_4Cl$ was used as friction materials.

The effects of velocity and load on the COF of the PVA/LiTFSI ionic hydrogel against the steel ball were also investigated. Figure 3d presents the COF under no applied electric field. When the velocity ranges from 0.05 to 10 mm $s^{-1}$, the COF gradually decreases as the load increases from 5 mN to 20 mN. This behavior is attributed to the elastic deformation of surface asperities.[50] Subsequently, as the load continues to increase to 70 mN, the COF exhibits an upward trend. This is generally attributed to the plastic deformation of asperities in contact.[50,51] In addition, the effect of velocity on the COF was also analyzed in detail. When the load is 5 mN, the COF initially increases with velocity and then decreases. However, at loads of 10–70 mN, the COF increases with increasing velocity, primarily because the viscous resistance in the contact zone rises as velocity increases. At higher contact pressures, an abnormally viscous flow is observed, leading to a sharp rise in viscosity due to the increase in velocity.[50] Figure 3e shows the COF under −30 V over time, with the same ranges of velocity and load as in Figure 3d. For different loads, the COF decreases with increasing velocity and then rises again. With increasing load, the COF decreases initially and then increases. By comparing the results in Figure 3d,e, under the same velocity and load, the COF or friction force without applying a voltage is 10–55 times higher than that obtained under a voltage of −30 V (Figure S23, Supporting Information).

Based on the effect of applied voltage on the COF and friction force, the power savings ($\Delta W$) resulting from the reduction in friction force before and after applying a −30 V voltage can be calculated using Equation (1).

$$\Delta W = \Delta\mu \cdot F_{load} \cdot v \tag{1}$$

where Δμ represents the difference between the COFs without applied voltage and that with −30 V applied, $F_{load}$ is the load, $v$ is the sliding velocity. Based on Equation (1), the power variation under different velocities and loads is shown in Figure 3f.

Given measured currents under an applied voltage of 1.5 V, the resistance of the ionic hydrogel (length: 14.85 mm, width: 4.09 mm, thickness: 0.28 mm) is calculated to be $(1.0 \pm 0.6) \times 10^8$ Ω. Accordingly, the power consumed for friction control under a −30 V applied voltage is estimated to be ≈ 9 μW. Comparing this value with the power savings shown in Figure 3f, it can be observed that as the sliding velocity and load increase, the power saved due to the reduction in the friction force caused by the applied electric field also increases. When the sliding velocity exceeds 2 mm $s^{-1}$, the saved power surpasses the consumed power (9 μW). At a velocity of 8 mm $s^{-1}$ and a load of 70 mN, the saved power reaches 538 μW, which is nearly 60 times the consumed power.

In addition, the relationship between the velocity/load and the COF under an applied voltage of −30 V is presented in Figure 3g, exhibiting characteristics consistent with the Stribeck curve for mixed or fluid lubrication.[52] In all the above cases, when −30 V is applied, the COF is consistently less than 0.05, and in most scenarios, it can be reduced to 0.02 or even lower, achieving an ultra-low friction state or even superlubricity state.

Figure 3h compares the present work with previous studies on electrotunable friction at the macroscopic scale. The x-axis indicates the year of publication, while the y-axis shows the range of variation in the COF achieved through electric field control. The earliest known demonstration of electric-field-controlled friction dates back to 1969.[53] In that pioneering study, friction between solids in a liquid electrolyte film was examined, revealing a tunable COF of 1.0–1.4. In 1994, H. A. Spikes and co-workers[27] examined the influence of electrochemical potentials on the friction and wear behaviors of iron/iron and iron oxide/alumina oxide contacts lubricated with aqueous fluids, achieving a tunable COF of 0.24–0.39. In 2010, Y. Meng and colleagues demonstrated potential-controlled friction of $ZrO_2$/stainless steel tribopairs in surfactant solutions, achieving COF tunability of 0.1–0.45 with response times of 0.2–1.5 s.[54] Moreover, by engineering the position and polarity of electrodes relative to the contact zone, they realized spatial control of friction.[55] Most conventional macroscopic investigations were conducted under liquid lubrication.[56] The base lubricants used for potential-controlled friction or electrotunable friction have expanded from aqueous solutions to non-aqueous systems.[26,28,57] Meanwhile, the electrically responsive additives have evolved from surfactants to ionic liquids,[19,58] micro- and nanoparticles,[59–62] as well as commercial anti-wear and friction modifiers.[57] Nevertheless, the majority of these systems achieve tunability within a relatively narrow COF range—typically between 0.1 and 0.3–0.4.[63,64] Additional details corresponding to Figure 3h can be found in Table S1 (Supporting Information).

Although the present study also falls under the category of macroscopic electrotunable friction, it fundamentally differs from previous work in both mechanism and performance. Here, we demonstrate electrotunable friction between ionic hydrogels and metal balls, without the need for external liquid lubrication. The COF is reversibly tunable from ultralow values (0.03) to dry contact levels (1-2)—corresponding to a tuning range 1–2 orders of magnitude greater than that achieved in any prior study. This highlights a significant advancement in the field of macroscale friction modulation via electrical control.

Figure 3i shows the COF response of PVA/LiTFSI versus steel ball to stepwise changes in voltage. When the voltage changes from 0 to −30 V, the COF decreases from 1.0–1.8 to ≈0.035. As the voltage returns to 0 V, the COF further decreases slightly to 0.022 and then gradually rises to ≈0.1 within 600 s. When the voltage is increased to +30 V, the COF rises sharply to 1.5–2.0 within ≈ 100 s. Upon removal of the voltage, the COF initially increases slightly and then decreases to ≈ 0.7. When −30 V is reapplied at

2400 s, the COF drops to ≈0.11 within 100 s. However, after disconnecting the voltage, the COF rises again to ≈ 2.0. In addition, for the tribo-pair of $NH_4Cl$ doped PVA-based ionic hydrogel and steel ball, the COF also varies as the voltage changes in steps. At −30 V, the COF decreases to ≈0.11 (Figure S24, Supporting Information), while at +30 V, it increases to 0.7–1.0. Fundamentally, the electrotunable friction mechanism depends on the ion mobility and polarization strength within the hydrogel network, rather than on the specific type of anion or metallic counterpart.

Furthermore, the wear on both the upper and lower friction pairs obtained under −30 V is negligible. Interestingly, a colorful, oil-film-like substance is observed on the uncleaned surface of the steel ball, as shown in Figure S25a (Supporting Information). After cleaning with water or ethanol, the wear track on the ionic hydrogel as well as the wear scar on the steel ball is found to be recoverable (Figure S25b, Supporting Information). When the PVA-based material is connected to the negative pole and the steel ball to the positive pole, the COF remains at 2.0, and significant wear is observed on the friction pairs (Figure S26, Supporting Information). Based on the above results, it is hypothesized that when the steel ball is connected to the negative pole and the ionic hydrogel to the positive pole, a lubricating boundary film forms on the frictional contact surface. Conversely, an oxide film forms on the frictional contact surface, particularly on the steel ball, resulting in a relatively high COF. Because metal oxides typically possess higher hardness, both adhesive and abrasive wear become more pronounced under these conditions, revealing a distinct coupling effect between electrochemical and mechanical wear. To avoid the irreversible effects on the friction interface caused by surface oxidation when the metal ball is connected to the positive pole, negative voltages and 0 V were used in the application scenarios to achieve reversible control of the friction behavior.

### 2.4. Mechanism Discussion of Eletrotunable Friction

Prior to discussing the mechanism of electrotunable friction, the electrical properties of the ionic hydrogel are first investigated. Figure S27a (Supporting Information) illustrates the relationship between conductivity and time for pure PVA and PVA/$LiTFSI_{50}$ under a 1.5 V voltage test. The results show that the conductivity of pure PVA is approximately 0.18 μS $m^{-1}$, while the conductivity of PVA/$LiTFSI_{50}$ increases significantly to ≈ 127.64 μS $m^{-1}$, which is consistent with the electrochemical impedance spectroscopy results (Figure S27b, Supporting Information). This demonstrates that the incorporation of LiTFSI into the hydrogel enhances ion transport efficiency and significantly improves conductivity. According to the cryo-scanning electron microscopy (cryo-SEM) observations in Figure S28 (Supporting Information), the cross-sectional observation of the sample reveals that the interior of the ionic hydrogel exhibits an oriented cross-linked network structure. The above electrical and microstructural characteristics provide the foundation for the electrotunable friction behavior of the ionic hydrogel.

To elucidate the influence of the applied electric field on ion transport, we constructed a dedicated simulation model. As shown in Figure S29 (Supporting Information), the electric field weakens $Li^+$-$TFSI^-$ ion pairing and promotes preferential coordination of $Li^+$ with oxygen sites on the PVA backbone, forming an electric-field-assisted ion-hopping pathway along the polymer chains. As a result, both $Li^+$ and $TFSI^-$ exhibit markedly enhanced mobility in the field direction, confirming that the electric field effectively facilitates ion migration within the hydrogel network.

Furthermore, to analyze the reasons for variations in the COF under different voltages and to uncover the microscopic mechanisms of electrotunable friction, we performed compositional and micro/nanostructural analyses of the wear scars on the upper friction pair (steel ball) and the wear tracks on the lower friction pair, as shown in **Figure 4**. First, an optical photothermal infrared (OPTIR, Figure 4a,b) spectroscopy was used to analyze the composition of the substance on the steel ball surface when the voltage was −30 V. On the ball surface, we identified points A and B, representing regions with a colorful lubricating boundary film, and points C and D, representing regions without the boundary film. Infrared spectra (Figure 4c) showed characteristic peaks near 1450 and 1260–1330 $cm^{-1}$ for points A and B, while no such peaks are observed at points C and D. Based on the analysis of the FTIR shown in Figure S4 (Supporting Information), the peaks near 1410–1460 $cm^{-1}$, 1327 $cm^{-1}$, and 1347 $cm^{-1}$ correspond to C—H bending, $\delta$(OH), rocking with CH wagging, and asymmetric $SO_2$ stretching, respectively. This indicates that the substances at points A and B are PVA/LiTFSI. Using 1450 $cm^{-1}$ as the characteristic wavelength, we mapped the distribution of substances within the box region in Figure 4a. As shown in Figure 4b, the regions corresponding to the colorful oil film exhibit a pronounced signal for this characteristic peak, while other areas show no significant signal.

The thickness and composition of the boundary film was analyzed using time-of-flight secondary ion mass spectrometry (TOF-SIMS), as shown in Figure 4d–h. Figure 4d demonstrates that as the sputtering depth increased (sputtering rate ≈0.142 nm $s^{-1}$), the concentration of $Li^+$ decreases gradually, while the concentration of Fe ions remains nearly constant. After 100 s of sputtering (≈14.2 nm depth), the $Li^+$ concentration stabilizes, indicating a Li-rich boundary film ≈ 14.2 nm thick. Figure 4e–g reveal that, in addition to Li, the boundary film also contains F and S, while Fe in Figure 4h originates from the steel ball. These results align with the findings in Figure 4a–c.

To analyze the valence states of the elements, we performed XPS on the wear tracks and wear scars obtained under different voltages. Figure 4i presents the XPS spectra of the wear tracks and wear scars under −30 and +30 V. For the wear track at −30 V, the detected elements include N, S, F, C, and O, where N, S, and F primarily originates from the additive LiTFSI. For the wear track at +30 V, the detected elements include Fe, F, O, C, N, and S. Among these, N, S, and F are mainly derived from LiTFSI, while Fe likely comes from the transfer of Fe ions or Fe oxides from the upper friction pair to the lower friction pair. For the wear scar at −30 V, the detected elements include F, O, N, C, and S, with N, S, and F primarily originating from LiTFSI, which constitutes the main components of the lubricating boundary film. For the wear scar at +30 V, the detected elements include Fe, O, N, and C, originating from iron oxides on the steel ball surface and substances transferred from the lower friction pair or absorbed from the atmosphere.

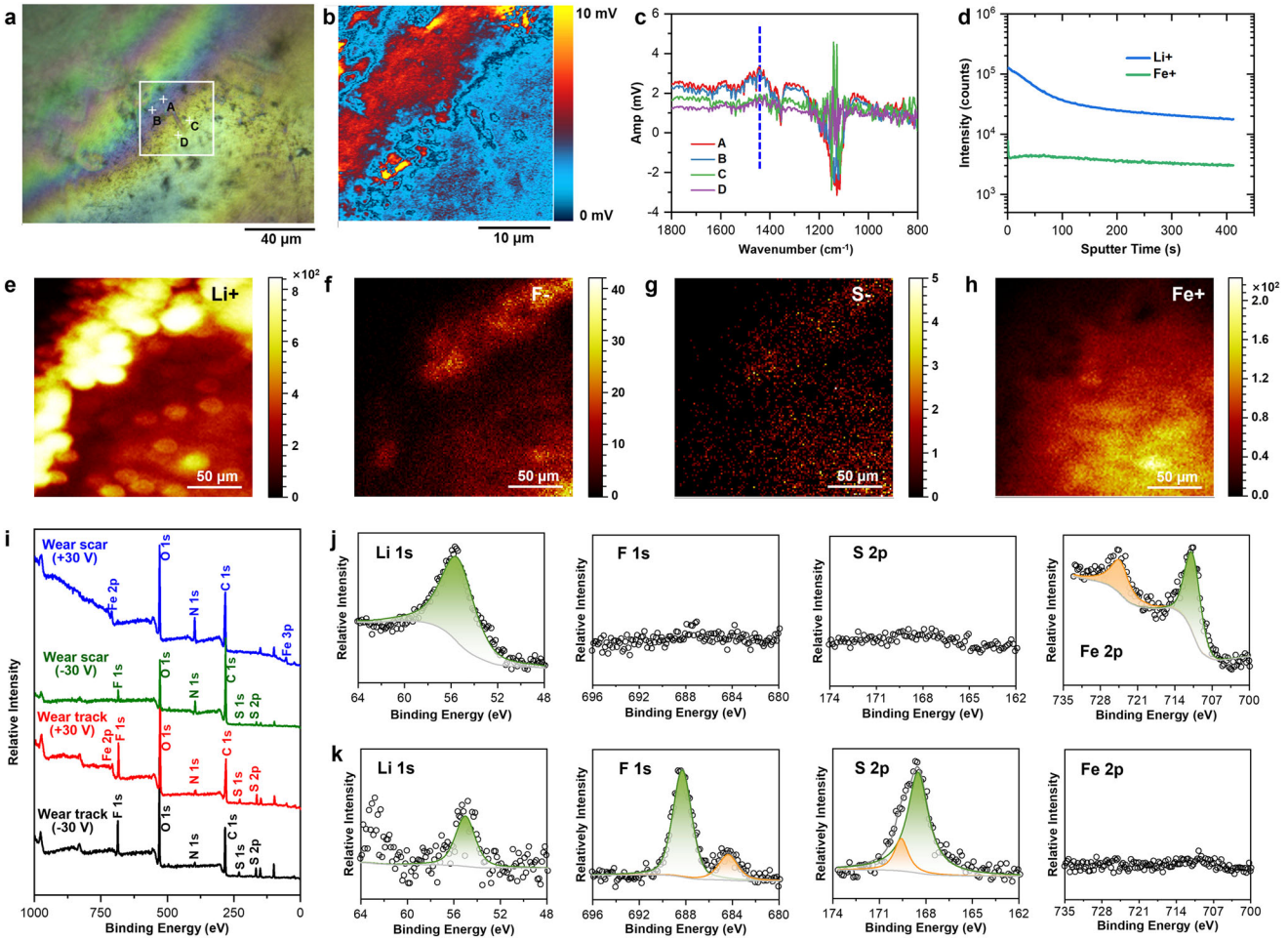


**Figure 4.** Compositional and structural characterization of wear scars on the steel ball and wear tracks on the ionic hydrogel after the friction tests under different voltages: a) Microscopic morphology of the wear scar on the steel ball surface at −30 V, along with surface distribution (b) and corresponding characteristic peaks (c); (d) TOF-SIMS results showing the depth-dependent composition of the wear scar on the steel ball surface after the friction test under −30 V; e–h) 2D TOF-SIMS mapping of Li, F, S, and Fe within the wear scar on the steel ball surface; i) XPS spectra of the wear tracks and wear scars under applied voltages of ±30 V; j) and k) XPS spectra of Li, F, S, and Fe in the wear scar on the steel ball surface at +30 and −30 V, respectively. The wear scars and wear tracks were obtained from friction experiments conducted for 600 s under a load of 20 mN and a sliding velocity of 2 mm $s^{-1}$.

Figure 4j further showed the valence states of the main elements on the steel ball surface after the friction test at +30 V. The characteristic peaks of Fe at 710.65 and 724.33 eV correspond to iron oxides, and the Li peak at 55.44 eV corresponds to the $Li^+$ from the LiTFSI. Figure 4k presents the valence state analysis of the steel ball surface after the friction test at −30 V. The characteristic peaks of S at 169.71 and 168.55 eV correspond to the sulfone group from the $TFSI^-$, Li at 55.44 eV corresponds to $Li^+$, and the characteristic peaks of F at 688.30 and 684.36 eV correspond to the trifluoromethyl group from the $TFSI^-$ and metal fluoride (e.g., LiF). Moreover, according to the XPS results of the wear tracks (Figure S30, Supporting Information), it is observed that when the steel ball acts as the positive electrode and underwent oxidation, Fe oxides are also detected at the wear track of the ionic hydrogel. This is attributed to frictional transfer. In contrast, when the steel ball serves as the negative electrode, no Fe is detected at the hydrogel's wear tracks. This result aligns with Figure S25 (Supporting Information), indicating that the damage caused by the steel ball to the hydrogel under −30 V is negligible.

As analyzed in Figure 2, $Li^+$ interacts with PVA, resulting in the existence of free $TFSI^-$.[65] In the absence of electric potential, the translational diffusion of the $TFSI^-$ at the molecular level can be described as random walks due to Brownian motion.[66] To further validate the lubricating effect of LiTFSI and to clarify whether the active contribution arises from the anion or the cation, a series of friction tests were conducted. **Figure 5a** shows the time-dependent variation of the COFs during friction tests on pure PVA lubricated with different liquids and paired with a steel ball. The results indicate that under pure water lubrication, the COF is around 0.148. However, when 1 M LiCl aqueous solution is used as the lubricant, the COF increases to 0.191. Conversely, with 1 M LiTFSI aqueous solution as the lubricant—where the cation ($Li^+$) type and concentration remain unchanged, but the anion shifts from $Cl^-$ to $TFSI^-$—the COF significantly decreases to ≈ 0.050. This demonstrates that the excellent lubrication performance is attributed to $TFSI^-$, not $Li^+$.

To further confirm the role of $TFSI^-$ anions, we studied the effect of salt concentration on the COF during sliding tests

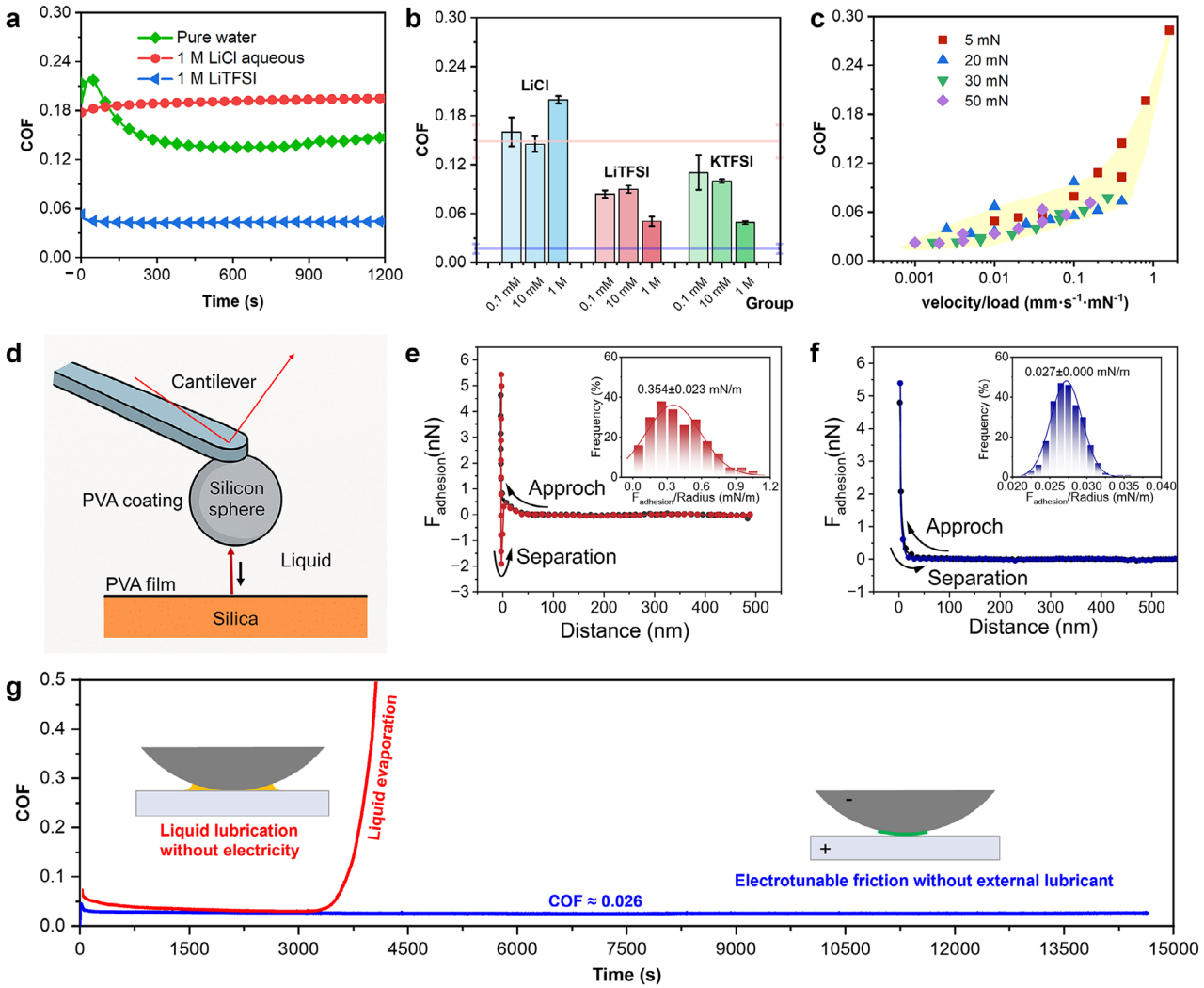


**Figure 5.** Mechanism of the electrotunable friction: a) Time-dependent variation of the COFs during friction tests on pure PVA lubricated with different liquids and paired with a steel ball; b) COF during sliding of pure PVA against the steel ball under lubrication with LiCl, LiTFSI, or KTFSI aqueous solutions of different concentrations; c) Relationship between COF and velocity/load under lubrication with 1 M LiTFSI aqueous solution at various velocities and loads; d) Schematic of AFM force measurement between PVA coatings in liquid, such as water or LiTFSI solution; Force histograms and representative force-distance curves in water (e), or in LiTFSI solution (f); g) Time-dependent variation of the COFs under two conditions: with liquid lubrication but no applied electric field, and with no liquid lubrication but an applied electric field. In the first case for (g), the friction pair consists of pure PVA and a steel ball, with 1 M LiTFSI aqueous solution (15 μL) as the lubricant; In the second case, the friction pair consists of PVA/LiTFSI$_{50}$ and a steel ball. The experiments were conducted under a load of 20 mN in (a), and 10 mN in (b) and (g), at a sliding velocity of 2 mm s$^{-1}$.

between pure PVA and the steel ball using various solutions (LiCl, LiTFSI, and KTFSI) as lubricants, as shown in Figure 5b. The experiments revealed the following trends: for LiCl solution, as the salt concentration increased from 0.1 mM to 1 M, the COF initially decreased slightly from 0.160 ± 0.018 to 0.145 ± 0.010, then increased to 0.199 ± 0.005. For LiTFSI solution, as the concentration increased from 0.1 mM to 1 M, the COF initially rose from 0.084 ± 0.004 to 0.090 ± 0.004, followed by a significant decrease to 0.050 ± 0.006. When the anion remained $TFSI^-$ but the cation was changed from $Li^+$ to $K^+$, increasing the KTFSI concentration from 0.1 mM to 1 M caused the COF to decrease from 0.110 ± 0.021 to 0.100 ± 0.002, then significantly further to 0.049 ± 0.002. These comparisons indicate that increasing the concentration of $Li^+$ does not reduce the COF, whereas increasing the concentration of $TFSI^-$ significantly reduces it.

The relationship between COF and velocity or load under lubrication with 1 M LiTFSI aqueous solution was studied, as shown in Figure 5c. The COF in these cases ranged from 0.03 to 0.12, slightly higher than the values in Figure 3g. However, the variation trends of COF with velocity and load are consistent between the two cases, further confirming that the anions in LiTFSI play a crucial role in the lubrication observed in electrotunable friction. At higher sliding velocities, the LiTFSI-enriched lubrication film thickens, leading to complete separation of the solid surfaces and a transition to viscous-dominated shear. Consequently, friction becomes governed by the hydrodynamic resistance of the confined lubrication film, resulting in an increase in COF with

velocity. Aaccording to the SFA results in Figures S31 and S32 (Supporting Information), when a PVA film comes into contact with mica or gold surfaces, the thickness of the LiTFSI lubrication film adsorbed on the PVA surface is 6.59 and 1.35 nm, respectively. These results provide evidence for the existence of a lubrication film.

To investigate the contribution of Li binding to the lubricity of LiTFSI, AFM force measurements were conducted using PVA-coated tips (Figure 5d). As shown in Figure 5e, the normalized adhesion force between the PVA-coated AFM tip and the PVA surface is 0.354 mN $m^{-1}$, likely originating from hydrogen bonding between —OH groups. In contrast, the adhesion force between PVA chains in LiTFSI solution decreases sharply to 0.027 mN $m^{-1}$, indicating that surface-adsorbed ions significantly weaken the interfacial interactions between PVA chains (Figure 5f).

Furthermore, the relationship between the COF and time was compared under two conditions: 1) with liquid lubrication but no applied electric field, and 2) with no liquid lubrication but with an applied electric field. In the first case, the friction pair consisted of pure PVA and a steel ball, with 1 M LiTFSI aqueous solution as the lubricant. In the second case, the friction pair consisted of PVA/$LiTFSI_{50}$ and a steel ball. As friction progressed, water in the aqueous solution gradually evaporated, leading to an increase in LiTFSI concentration. This concentration rise reduced the COF, consistent with the concentration-COF relationship shown in Figure 5b. However, as evaporation continued and the system transitioned toward dry contact, the absence of sufficient liquid film caused the COF to increase sharply due to direct solid-solid interaction. Consequently, over the full sliding duration of this case, the COF first decreased and then increased rapidly to above 0.5, resulting in the trend observed in Figure 5g. In contrast, for the condition without liquid lubrication but with electric field regulation (at −30 V), the COF remained stable at ≈0.026 throughout the experiment, without a noticeable running-in period. Moreover, the latter approach eliminates concerns about lubricant leakage and corrosion, offering not only superior friction reduction and wear resistance but also broader applicability across various scenarios.

### 2.5. Application Exploration of Electrotunable Friction

To explore the potential of this frictional system for crawling robots, ship launching operations, and other applications requiring friction control, we conducted a series of macroscopic demonstration experiments. A titanium alloy block (25 mm in diameter and 7 mm thick), coated on the bottom surface with a PVA/$LiTFSI_{50}$ film, was used as the sliding block, while a smooth tin foil sheet served as the sliding track. The titanium alloy was connected to the anode of a direct current (DC) power supply, and the tin foil to the cathode. The applied voltage was adjusted from 0 up to 20 V. By varying the tilt angle between the sliding track and the horizontal plane, we achieved stable sliding motion of the block along the inclined tin surface. **Figure 6a** illustrates the sliding process of a titanium alloy slider coated with PVA/$LiTFSI_{50}$ on a tin foil surface, while Figure 6b shows the effect of the electric field on the sliding behavior. In the absence of an electric field, the slider remained stationary even on a 70° incline and only began to slide when the slope angle reached 76°. In contrast, the introduction of a DC electric field enabled the block to slide on an 8° incline (Video S1, Supporting Information), demonstrating that the electric field could significantly reduce the static friction between the slider and the track.

The above strategy for controlling friction and the COF can be extended to practical applications. For instance, in the ship-launching model (Figure 6c; Video S2, Supporting Information), the bottom of the ship is coated with PVA-LiTFSI (Figure S33a, Supporting Information). By applying an external electric field (−32 V for the metal slide), we regulated the friction between the ship and the metal slide, enabling a smooth entry of the ship into the water. The advantage of this method lies in the real-time tunability of friction through the applied electric field, thereby avoiding abrupt frictional changes that might otherwise damage the ship.

Similarly, in robotic gripping and releasing (Figure 6d,e; Videos S3 and S4, Supporting Information), using "normal force control" alone (i.e., simply relaxing the grip) often causes objects—such as the soda bottle in Figure 6d—to drop abruptly. As shown by the blue curve in Figure 6f, the object undergoes free-fall motion under gravity, with its drop height and time following a near-parabolic trajectory. In contrast, by applying an external electric field to regulate the COF between the robotic gripper (coated with PVA-LiTFSI) and the soda bottle (termed "COF control"), the release process becomes gradual. The red curve in Figure 6f demonstrates a more controllable descent compared with the blue curve. This type of robotic gripper is particularly suited for precise and reversible grasping, allowing delicate handling of fragile objects such as bottles or electronic components.

More importantly, electrically regulated friction enables locomotion of a crawling robot (Figure 6g,h; Video S5, Supporting Information). The robot comprises block 1, block 2, and a telescopic brake. One cycle of telescopic electrode actuation takes ≈2.7 s. Both blocks are coated at their bases with Cu conductive tape and PVA-LiTFSI (Figure S33b, Supporting Information), while a DC power supply alternately applies positive and negative voltages between block 2 and an aluminum track. When PVA-LiTFSI is connected as the anode and the track as the cathode, the COF is reduced, and the friction force between block 1 and the track ($F_1$) becomes smaller than that of block 2 ($F_2$). In this case, block 1 advances forward, while block 2 and the telescopic brake (the red point in the gray region) remain nearly stationary. After voltage reversal, $F_1$ exceeds $F_2$, leading block 2 and the telescopic brake to move leftward while block 1 remains nearly still. Through this alternating process, the robot achieves crawling locomotion. The displacement-time curve of the worm robot's center in the horizontal direction (Figure 6i) shows that after three actuation cycles (≈8 s), the robot achieves a net displacement of 1.5 cm. This work presents the first demonstration of a crawling robot powered by externally applied electric fields to regulate the COF and frictional force, marking a transformative step toward adaptive and energy-efficient robotics. Meanwhile, this approach could extend to smart tactile interfaces, haptic feedback systems, and self-adaptive mechanical surfaces for next-generation robotics and wearable technologies.

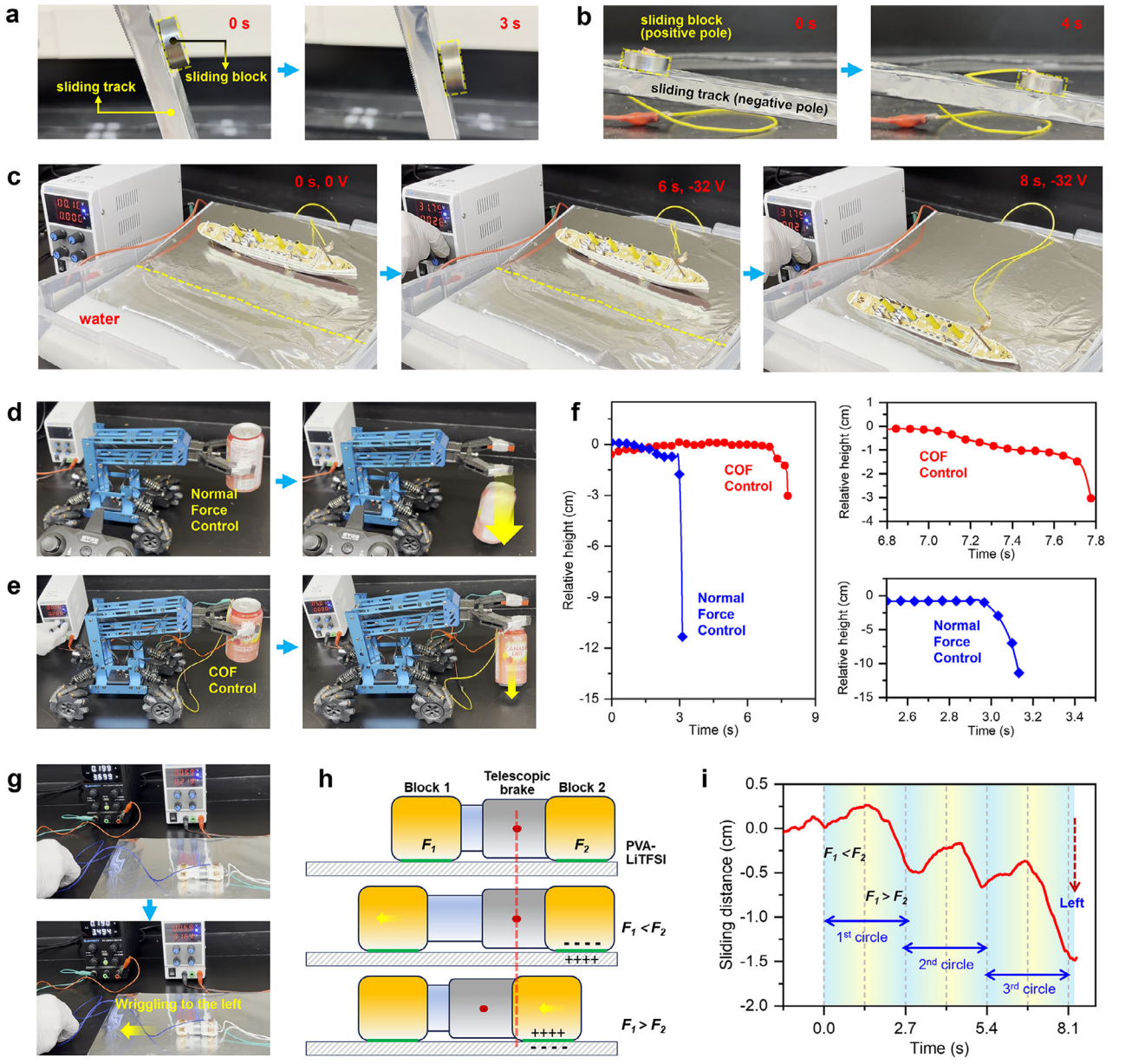


**Figure 6.** Potential applications of the electrotunable friction. a) Sliding process of a titanium alloy slider coated with PVA/LiTFSI$_{50}$ on a tin foil surface, and b) the effect of an electric field on the sliding behavior. For the latter case, the titanium alloy slider coated with PVA/LiTFSI$_{50}$ served as the positive electrode, and the sliding track as the negative electrode; c) Electrically controlled sliding of a ship model with a PVA/LiTFSI$_{50}$-coated base on a metal surface into water, simulating ship launching; d,e) Photographs of robotic gripping and releasing of a soda bottle, regulated either by controlling the normal load (d) or by applying an external electric field to tune the COF (e). In (d), the release process was realized by adjusting the relative displacement of the gripper arms to modulate the normal load. In (e), the soda bottle served as the cathode, the PVA-LiTFSI coated robotic gripper as the anode, with an applied voltage of 32 V; f) Relative height-time curves of the soda bottle release process for the two cases, with the enlarged details; Photograph (g) and schematic (h) of a crawling robot driven by electrorunable friction. The robot consists of block 1, block 2, and a telescopic brake, with one cycle of telescopic electrode actuation taking ≈2.7 s. Both block 1 and block 2 were coated at the bottom with Cu conductive tape and a PVA-LiTFSI layer. A DC voltage of 18 V was alternately applied between block 2 and an aluminum track; i) Relative horizontal displacement of the worm robot's center as a function of time.

## 3. Conclusion

This study demonstrates a groundbreaking approach to electrotunable friction, achieving a more-than-fifty-fold modulation of the COF between the ionic hydrogel (PVA/LiTFSI$_{50}$) and metals at macroscopic scales. By applying an electric field, the COF can be reduced from traditional dry friction to the ultra-low friction range, reaching values as low as 0.03. Notably, this process also ensures that wear tracks on the ionic hydrogel are recoverable after cleaning with water and ethanol.

In contrast to conventional strategies for macroscopic electrotunable friction, the regulation in this work is achieved without the need for external liquid lubricants. This eliminates sealing issues and weakens the risk of material corrosion, thereby greatly expanding its potential application scenarios. The mechanism underlying this phenomenon involves the electroosmotic extraction of LiTFSI salt, which form a lubricating film on the friction pairs under a negative electric field, leading to a substantial reduction in COF. This innovative approach not only provides new insights into the mechanisms of electrotunable friction but also opens promising applications in fields such as ship launching, and robotic arm manipulation. In particular, this work presents the first crawling robot powered by electric-field regulation of friction, which minimizes surface wear and provides a new paradigm for lightweight, modular, and energy-efficient robotic systems.

## 4. Experimental Section

All details are presented in the Supporting Information.

## Supporting Information

Supporting Information is available from the Wiley Online Library or from the author.

## Acknowledgements

C.L. and Y.Y. contributed equally to this work. This work has been financially supported by the Natural Sciences and Engineering Research Council of Canada and the Canada Research Chairs Program.

## Conflict of Interest

The authors declare no conflict of interest.

## Data Availability Statement

The data that support the findings of this study are available from the corresponding author upon reasonable request.

## Keywords

crawling robots, electric field, friction control, ionic polymers, ultra-low friction

Received: September 17, 2025
Revised: November 18, 2025
Published online:

[1] C. Du, T. Yu, X. Sui, Z. Zhang, R. Cai, L. Zhang, Y. Feng, M. Feng, F. Zhou, D. Wang, *Adv. Mater.* **2024**, *37*, 2413781.
[2] L. Wang, L. Zhang, C. Du, T. Yu, M. Feng, X. Zhang, W. Bu, D. Wang, F. Zhou, *ACS Nano* **2024**, *18*, 34288.
[3] K. Holmberg, A. Erdemir, *Friction* **2017**, *5*, 263.
[4] Y.i Zhang, H. Chen, K. Gao, Y. Li, J. Jiao, G. Xie, J. Luo, *Adv. Funct. Mater.* **2024**, *34*, 2401143.
[5] L.i Xiang, Y. Zhang, Z. Zhao, Y.i Tao, W. Wang, J. Liu, Y. Chen, J. Jiang, J. Zhang, H. Zeng, *ACS Nano* **2024**, *19*, 1316.
[6] Y.u Zhang, D.i Jin, R. Tivony, N. Kampf, J. Klein, *Nat. Mater.* **2024**, *23*, 1720.
[7] J. Li, C. Zhang, J. Luo, *Langmuir* **2011**, *27*, 9413.
[8] T. Wang, Y. Wang, X. Wang, B. He, S. Liu, Q. Ye, F. Zhou, W. Liu, *ACS Nano* **2024**, *18*, 33468.
[9] O. Hod, E. Meyer, Q. Zheng, M. Urbakh, *Nature* **2018**, *563*, 485.
[10] X. Gao, W. Ouyang, M. Urbakh, O. Hod, *Nat. Commun.* **2021**, *12*, 5694.
[11] C. Qu, K. Wang, J. Wang, Y. Gongyang, R. W. Carpick, M. Urbakh, Q. Zheng, *Phys. Rev. Lett.* **2020**, *125*, 126102.
[12] V. Slesarenko, L. Pastewka, *Science* **2024**, *383*, 150.
[13] S. Glavatskih, E. Höglund, *Tribol. Int.* **2008**, *41*, 934.
[14] S. Tang, S. Li, S. Zhu, L. Ma, Y.u Tian, *Tribol. Int.* **2022**, *176*, 107914.
[15] J. Krim, *Front. Mechan. Eng.* **2019**, *5*, 00022.
[16] F. Bresme, A. A. Kornyshev, S. Perkin, M. Urbakh, *Nat. Mater.* **2022**, *21*, 848.
[17] A. S. de Wijn, A. Fasolino, A. E. Filippov, M. Urbakh, *Phys. Rev. Lett.* **2014**, *112*, 055502.
[18] C. Drummond, *Phys. Rev. Lett.* **2012**, *109*, 154302.
[19] F. Gatti, T. Amann, A. Kailer, N. Baltes, J. Rühe, P. Gumbsch, *Sci. Rep.* **2020**, *10*, 17634.
[20] X. Zhou, Z. Xiang, P. Bai, X. Wen, C. Dong, C. Liu, Y. Li, S. Zhu, Y. Meng, Y. Tian, *Tribol. Int.* **2024**, *194*, 109487.
[21] Y. Zhang, M. W. Rutland, J. Luo, R. Atkin, H. Li, *J. Phys. Chem. C* **2021**, *125*, 3940.
[22] S. Li, P. Bai, Y. Li, N. S. Pesika, Y. Meng, L. Ma, Y.u Tian, *Friction* **2020**, *9*, 513.
[23] H. A. Spikes, *Tribology Lett.* **2020**, *68*, 90.
[24] A. Labuda, F. Hausen, N. N. Gosvami, P. H. Grütter, R. B. Lennox, R. Bennewitz, *Langmuir* **2011**, *27*, 2561.
[25] T. Gao, J. Li, S. Yi, J. Luo, *J. Phys. Chem. C* **2020**, *124*, 23745.
[26] R. Dong, L. Bao, Q. Yu, Y. Wu, Z. Ma, J. Zhang, M. Cai, F. Zhou, W. Liu, *ACS Appl. Mater. Interfaces* **2020**, *12*, 39910.
[27] Y. Y. Zhu, G. H. Kelsall, H. A. Spikes, *Tribol. Trans.* **1994**, *37*, 811.
[28] A. Borchers, T. Pieler, *Lubricants* **2022**, *10*, 413.
[29] T. Wang, M. Farajollahi, Y. S. Choi, I.-T. Lin, J. E. Marshall, N. M. Thompson, S. Kar-Narayan, J. D. W. Madden, S. K. Smoukov, *Interface Focus* **2016**, *6*, 20160026.
[30] J. Wen, J. Tang, H. Ning, N. Hu, Y. Zhu, Y. Gong, C. Xu, Q. Zhao, X. Jiang, X. Hu, L. Lei, D. Wu, T. Huang, *Adv. Funct. Mater.* **2021**, *31*, 2011176.
[31] B. Adhikari, S. Majumdar, *Prog. Polym. Sci.* **2004**, *29*, 699.
[32] W. Gao, S. Emaminejad, H. Y. Y. Nyein, S. Challa, K. Chen, A. Peck, H. M. Fahad, H. Ota, H. Shiraki, D. Kiriya, D.-H. Lien, G. A. Brooks, R. W. Davis, A. Javey, *Nature* **2016**, *529*, 509.
[33] G. Gu, J. Zou, R. Zhao, X. Zhao, X. Zhu, *Sci. Rob.* **2018**, *3*, aat2874.
[34] Y. Hu, L. Yang, Q. Yan, Q. Ji, L. Chang, C. Zhang, J. Yan, R. Wang, L. Zhang, G. Wu, J. Sun, B. Zi, W. Chen, Y. Wu, *ACS Nano* **2021**, *15*, 5294.
[35] Y. Li, P. Bai, H. Cao, L. Li, X. Li, X. Hou, J. Fang, J. Li, Y. Meng, L. Ma, Y. Tian, *Sci. Adv.* **2022**, *8*, abm0984.
[36] S. Kim, Y. Cha, *iScience* **2023**, *26*, 106726.
[37] D. Wang, S. Zhao, R. Yin, L. Li, Z. Lou, G. Shen, *npj Flexible Electron.* **2021**, *5*, 13.
[38] M. Teodorescu, M. Bercea, S. Morariu, *Biotechnol. Adv.* **2019**, *37*, 109.
[39] R. J. Sengwa, V. K. Patel, M. Saraswat, *J. Polym. Res.* **2022**, *29*, 480.
[40] I. Jipa, A. Stoica, M. Stroescu, L.-M. Dobre, T. Dobre, S. Jinga, C. Tardei, *Chem. Pap.* **2012**, *66*, 138.
[41] S.-Y. Lin, W.-T. Cheng, Y.-S. Wei, H.-L. Lin, *Polym. J.* **2011**, *43*, 577.
[42] I. Rey, J. C. Lassègues, J. Grondin, L. Servant, *Electrochim. Acta* **1998**, *43*, 1505.

[43] L. Xu, S. Gao, Q. Guo, C. Wang, Y. Qiao, D. Qiu, *Adv. Mater.* **2020**, *32*, 2004579.
[44] S. G. Rathod, R. F. Bhajantri, V. Ravindrachary, T. Sheela, P. K. Pujari, J. Naik, B. Poojary, *J. Polym. Res.* **2015**, *22*, 6.
[45] C. Tang, Y. Yao, M. Li, Y. Wang, Y. Zhang, J. Zhu, L. Wang, L. Li, *Adv. Funct. Mater.* **2024**, *35*, 2417207.
[46] Y. Zhao, D. Wang, Y. Gao, T. Chen, Q. Huang, D. Wang, *Nano Energy* **2019**, *64*, 103893.
[47] S. T. C. L. Ndruru, M. Y. Saputra, Z. Zurriyati, A. T. Hayati, R. Adriana, M. A.l Muttaqii, E. Pramono, S. Widiarto, M. H. Pasaribu, B. A. Widyaningrum, R. W. N. Nugroho, D. Wahyuningrum, I. M. Arcana, *J. Appl. Polym. Sci.* **2024**, *141*, 56050.
[48] X. Dong, W. Chen, X. Ge, S. Li, Z. Xing, Q. Zhang, Z.-X. Wang, *J. Energy Storage* **2024**, *89*, 111793.
[49] Q. Zheng, D. M. Pesko, B. M. Savoie, K. Timachova, A. L. Hasan, M. C. Smith, T. F. Miller, G. W. Coates, N. P. Balsara, *Macromolecules* **2018**, *51*, 2847.
[50] N. K. Myshkin, M. I. Petrokovets, A. V. Kovalev, *Tribol. Int.* **2005**, *38*, 910.
[51] I. V. Kragelsky, M. N. Dobychin, V. S. Kombalov, *Friction and Wear Calculation Methods*, Pergamon Press, New York **1982**.
[52] S. Wen, *Principles of Tribology*, Wiley, Hoboken, New Jersey **2017**.
[53] J. O. M. Bockris, S. D. Argade, *J. Chem. Phys.* **1969**, *50*, 1622.
[54] S. He, Y. Meng, Y. Tian, Y. Zuo, *Tribol. Lett.* **2010**, *38*, 169.
[55] J. Zhang, Y. Meng, X. Yu, *Tribology Letters* **2015**, *59*, 43.
[56] Q. Chang, Y. Meng, S. Wen, *Appl. Surf. Sci.* **2002**, *202*, 120.
[57] C. Liu, W. Li, C. Ouyang, Y. Tian, Y. Meng, *Tribol. Lett.* **2022**, *70*, 19.
[58] C. Dold, T. Amann, A. Kailer, *Phys. Chem. Chem. Phys.* **2015**, *17*, 10339.
[59] C. Liu, Y. Meng, Y. Tian, *Tribol. Lett.* **2020**, *68*, 72.
[60] C. Liu, O. Friedman, Y. Li, S. Li, Y. Tian, Y. Golan, Y. Meng, *Langmuir* **2019**, *35*, 15825.
[61] C. Liu, O. Friedman, Y. Meng, Y. Tian, Y. Golan, *ACS Appl. Nano Mater.* **2018**, *1*, 7060.
[62] Y. Guo, L. Zhang, G.a Zhang, D. Wang, T. Wang, Q. Wang, *J. Mater. Chem. A* **2018**, *6*, 2817.
[63] C. Liu, Y.u Tian, Z. A. Khan, Y. Meng, *Friction* **2023**, *11*, 801.
[64] C. Liu, J. Fang, X. Wen, Y. Tian, Y. Meng, *Tribol. Lett.* **2021**, *69*, 144.
[65] J. Wang, Z. Zhao, S. Song, Q. Ma, R. Liu, *Polymers (Basel)* **2018**, *10*, 1179.
[66] Y. Choo, D. M. Halat, I. Villaluenga, K. Timachova, N. P. Balsara, *Prog. Polym. Sci.* **2020**, *103*, 101220.